Diapycnal and Isopycnal Transports in the Southern Ocean Estimated by a Box Inverse Model

K. KATSUMATA

RIGC JAMSTEC, Yokosuka, Japan

B. M. SLOYAN

Centre for Australian Weather and Climate, CSIRO, and CSIRO Wealth from Ocean National Research Flagship, Hobart, Tasmania, Australia

S. MASUDA

RIGC JAMSTEC, Yokosuka, Japan

(Manuscript received 21 October 2012, in final form 9 May 2013)

ABSTRACT

Quantitative descriptions of Circumpolar Deep Water upwelling and evolution into a lighter mode and heavier bottom waters in the Southern Ocean are still not well constrained. Here, data from two occupations of eight hydrographic sections are combined and used in a box inverse model to estimate isopycnal and diapycnal transports in the Southern Ocean. A mixed layer box allows diapycnal transports in the surface mixed layer to be estimated separately. Current velocity at 1000 dbar was constrained by the mean velocity field estimated from subsurface float drift data. The estimated isopycnal transports are largely consistent with past estimates and with outputs of three ocean general circulation models. The estimated subduction and upwelling at the base of the Southern Ocean mixed layer show that Upper Circumpolar Deep Water upwells [16 ± 15 and 17 ± 21 Sv (where $1\,\text{Sv} \equiv 10^6\,\text{m}^3\,\text{s}^{-1}$) by different inversion methods] and evolves into heavier Lower Circumpolar Deep Water (5 ± 13 and 6 ± 18 Sv) and Bottom Water (8 ± 9 and 8 ± 13 Sv) or lighter Mode and Intermediate Waters (9 ± 18 and 13 ± 24 Sv). Meridional transport in the surface mixed layer is due to northward Ekman transport and mostly southward eddy transport. In seasonal ice-covered areas near Antarctica, a significant (14 ± 14 Sv) southward transport was found. The southward eddy transport is largest north of the Antarctic Circumpolar Current and decreases poleward because of the poleward decrease in the eddy diffusivity. The interior diapycnal transports, which can be either upward (gaining buoyancy) or downward (gaining density), are comparable in magnitude to the horizontal diapycnal transports within the surface mixed layer.

1. Introduction

The Southern Ocean is one of only two latitude bands in the global meridional overturning circulation where surface waters gain density to become bottom waters (Jacobs 2004). Recently accumulated evidence (e.g., Toggweiler and Samuels 1998; Speer et al. 2000; Webb and Suginohara 2001; Hallberg and Gnanadesikan 2006) points to another central role of the Southern Ocean as a return pathway of bottom water to the surface (Marshall and Speer 2012). Upwelling of deep waters in the Atlantic, Indian, and Pacific sectors of the Southern Ocean is largely driven by the westerly winds over the ocean. Some of this upwelled water flows equatorward to evolve into mode and intermediate waters, while the rest flows poleward to become bottom water.

Box inverse models have been used to estimate the volume transport of this upwelling (Macdonald and Wunsch 1996; Ganachaud and Wunsch 2000; Sloyan and Rintoul 2001b; Lumpkin and Speer 2007). The hydrographic data used in these inverse models are mainly from the World Ocean Circulation Experiment (WOCE) Hydrographic Program (WHP). The estimated circulations agree grossly but exhibit some differences (e.g., these studies estimate the southward temperature flux across

Corresponding author address: K. Katsumata, RIGC JAMSTEC, 2-15 Natsushima, Yokosuka, 2370061 Japan.
E-mail: k.katsumata@jamstec.go.jp

DOI: 10.1175/JPO-D-12-0210.1

the Indian Ocean at 32°S to be 1.3, 1.5, 0.87, and 1.55 PW, respectively), reflecting the different assumptions and constraints of the models. Since the WOCE occupation, some of these hydrographic sections have been reoccupied to elucidate long-term variabilities in water masses and circulation (e.g., Rintoul and Sokolov 2001; Johnson et al. 2007; Katsumata and Fukasawa 2011). In this paper, we update previous Southern Ocean circulation estimates by combining these two sets of hydrographic data. Since 2000, the hydrographic sections account for only a small portion of increased data from the Southern Ocean; Argo profiling floats have dramatically increased the total amount of hydrographic data (0–2000 m) from the Southern Ocean (Roemmich 2007). In this work, we also use the velocity estimates derived from the Argo drift data (Katsumata and Yoshinari 2010) to constrain velocity across hydrographic sections (Wijffels et al. 2001; Hernández-Guerra et al. 2010). We also compare the estimated circulation determined by the box inverse model with three ocean general circulation models (OGCMs).

The observation-based inverse models and OGCMs both show a middepth upwelling branch of the meridional overturning circulation. The overturning circulation is closed by buoyancy loss or gain either in the ocean surface mixed layer or ocean interior. The relative importance of surface or interior processes in closing the overturning circulation is difficult to quantify, largely because of the paucity of data. Nevertheless, quantitative description of these mixing processes is important for understanding the complex physics of the Southern Ocean and answering the closely linked and long-standing question as to what drives the global meridional overturning circulation (Kuhlbrodt et al. 2007; Naveira Garabato et al. 2007). Idealized models of Southern Ocean meridional circulation (e.g., Marshall and Radko 2003; Olbers and Visbeck 2005) often assume that the interior Southern Ocean, below the surface mixed layer, is adiabatic and that all diapycnal fluxes are concentrated near the surface. Recent in situ observation (Naveira Garabato et al. 2004) and some numerical simulations (Iudicone et al. 2008a,b) suggest that these idealistic assumptions may not be justified. A goal of this work, therefore, is to estimate diapycnal transport in both the surface mixed layer and interior ocean.

The convergence and divergence of diapycnal transport in the surface mixed layer drive water mass subduction and upwelling, respectively. Sallée et al. (2010) estimated subduction/upwelling as well as diapycnal transport in the surface mixed layer and determined the relative importance of Ekman and eddy transports on mixed layer processes, but the southern limit of their estimate was the seasonal ice edge. Here, we attempted to extend the southern limit of mixed layer subduction/upwelling estimates by using hydrographic data. An advantage of this study is that our estimate is free from assumptions about the mixing process, such as horizontal eddy-mixing coefficients, sea ice processes, and poorly constrained (Cerovečki et al. 2011) air–sea flux data. On the other hand, the hydrographic sections in the Southern Ocean were observed during summer, and possible seasonal biases have to be accounted for by large uncertainties. Also the spatial resolution of box inverse models is much lower than that of Argo- or satellite-based analyses (Sallée et al. 2010, 2011).

2. Box inverse model

Eight hydrographic sections define the horizontal extent of the boxes (Fig. 1 and Table 1), which are separated vertically by neutral density surfaces: the sea surface, γ^n = 26.0, 26.1, 26.2, 26.3, 26.4, 26.5, 26.6, 26.7, 26.8, 26.9, 27.0, 27.1, 27.2, 27.3, 27.4, 27.5, 27.6, 27.72, 27.8, 27.9, 28.0, 28.11, and 28.2, and the sea floor, where γ^n denotes the approximate neutral density of $(1000 + \gamma^n)$ kg m^{-3} calculated by the method of Jackett and McDougall (1997). Following Sloyan and Rintoul (2001b), we label the water masses according to their neutral density (Table 2).

In the inverse models used in this study, the transport between landmasses was not constrained except for the Bering Throughflow, which was constrained at 0.8 ± 0.3 Sv [1 Sv ≡ 10^6 m^3 s^{-1}; Roach et al. (1995)]. Geostrophic velocity across the sections with assumed zero-velocity surfaces was calculated from measured temperature and salinity values with the new Thermodynamic Equation of Seawater—2010 (TEOS-10, Intergovernmental Oceanographic Commission 2010). The initial zero-velocity surfaces were at γ^n = 28.05, 28.1, and 28.15 for the zonal sections in the Pacific, Indian, and Atlantic Oceans, respectively, and at the bottom for the meridional sections except for γ^n = 28.318 for the SR3 section. The velocity correction at these initial zero-velocity surfaces and the diapycnal fluxes were then determined such that the volume, temperature, and salinity in each box were conserved. Details of the inverse box model are described in the appendix. The present box model is similar to previous box models (e.g., Ganachaud and Wunsch 2000; Sloyan and Rintoul 2001b) but with three major differences, described in sections 2a–c.

a. Mixed layer box

We included a surface ''mixed layer'' box in the inverse model that is separate from the interior boxes (Fig. 2). Each large basin box, defined by the hydrographic sections, is divided into a surface and interior boxes, and volume and tracers can be exchanged between the surface

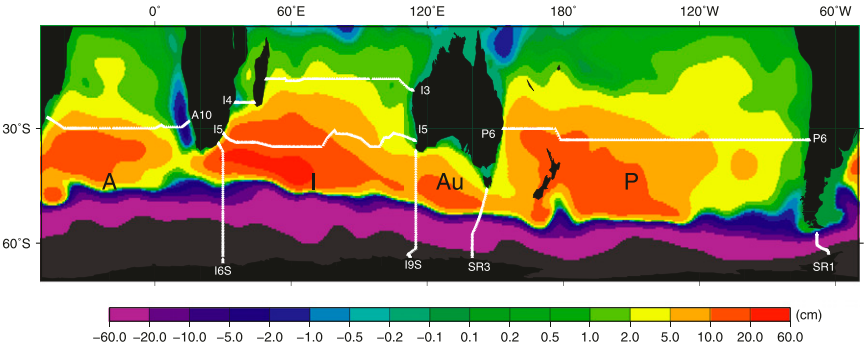

FIG. 1. Hydrographic sections defining the boxes. The hydrographic sections (Table 1) are indicated by white lines and labeled using white type. Black type is used to label the sectors of the Southern Ocean: Atlantic sector (A), Indian sector (I), Australian sector (Au), and Pacific sector (P). The color scale shows the geostrophic pressure (centimeters of water column) at 1000 dbar estimated from WOCE subsurface (Davis 1998, 2005) and Argo (Katsumata and Yoshinari 2010) drift data.

and interior boxes in the same basin as well as with adjoining basin surface boxes. The separation of the surface and interior ocean is motivated by theoretical models of the Southern Ocean meridional circulation (e.g., Marshall and Radko 2003; Olbers and Visbeck 2005), in which it is assumed that the overturning circulation is driven by near-surface momentum and buoyancy fluxes from the atmosphere whereas the interior is adiabatic, and by observational studies suggesting that the interior ocean mixing is an important component of the Southern Ocean meridional circulation (e.g., Sloyan and Rintoul 2001a,b; Naveira Garabato et al. 2004).

By defining a separate mixed layer box and interior ocean box, we can distinguish the near-surface diapycnal fluxes driven by surface buoyancy forcing and eddies from the interior diapycnal fluxes driven by diapycnal mixing from breaking gravity waves and nonlinear effects of the seawater equation of state. Subduction and upwelling through the base of the mixed layer are estimated as part of the inverse solution. The thickness of the mixed layer is defined by density; the bottom of the mixed layer box is at the depth where the density is $0.03\,\mathrm{kg\,m^{-3}}$ heavier than the surface density defined as the average density above the 20-dbar depth (Dong et al. 2008).

FORMULATION

To define the mixed layer box in the inverse model, we consider the volume budget of the mixed layer (Sallée et al. 2010)

$$S = \frac{\partial H}{\partial t} + \nabla \int_{-H}^{0} \mathbf{u}\, dz, \tag{1}$$

where S is the rate at which water crosses the mixed layer base (positive is upwelling into the mixed layer),

TABLE 1. Hydrographic sections. Unless otherwise noted, data were downloaded from the Climate Variability and Predictability (CLIVAR) and Carbon Hydrographic Data Office (CCHDO) website (http://cchdo.ucsd.edu/). Parentheses around S03 indicate that only a small amount of data was used from this source.

Section	Lat/lon	WHP cruise	Reference	Revisit cruise	Reference
P06	32.5°S	May–Jul 1992	Tsimplis et al. (1998)	Aug–Oct 2003	Katsumata and Fukasawa (2011)
I3/4	20°S	Apr–Jun 1995	CCHDO[a]	Dec 2003–Jan 2004	Katsumata and Fukasawa (2011)
I5	34°S	Nov–Dec 1987	Toole and Warren (1993)	Mar–May 2009	CCHDO[a]
A10	30°S	Dec 1992–Jan 1993	Siedler et al. (1996)	Nov–Dec 2003	Katsumata and Fukasawa (2011)
I6S	30°E	Feb–Mar 1996	CCHDO[a]	Feb–Mar 2008	CCHDO[a]
I9S[b]	115°E	Jan 1995	McCartney and Donohue (2007)	Dec 2004–Jan 2005	CCHDO[a]
(S03)	—	Mar 1995	Rintoul and Sokolov (2001)	—	—
SR1[c]	68°W	Jan 1990	Roether et al. (1993)	Feb 2009	McDonagh (2009)
SR3	140°E	Jan 1994	Rintoul and Sokolov (2001)	Mar–Apr 2008	CCHDO[a]

[a] We were unable to locate references other than the cruise reports (http://cchdo.ucsd.edu).
[b] To fill the data gap on the Antarctic Shelf for the WHP cruise, stations 7–10 from the WHP S03 cruise (expo code 09AR9404) were added.
[c] Revisit data are available on request (http://www.bodc.ac.uk/).

TABLE 2. Water mass definition.

Water mass	Neutral density
Thermocline Water (TW)	$\gamma^n < 26.0$
Intermediate Water (IW)	$26.0 < \gamma^n < 27.4$
Upper Circumpolar Deep Water (UCDW or UW)	$27.4 < \gamma^n < 28.0$
Lower Circumpolar Deep Water (LCDW or LW)	$28.0 < \gamma^n < 28.2$
Bottom Water (BW)	$28.2 < \gamma^n$

H is the mixed layer depth, and $\mathbf{u}$ is the horizontal velocity in the mixed layer. Integration of (1) in an area A between basin-bounding hydrographic sections and two isopycnals gives

$$\int_A S\,da = \int_A \frac{\partial H}{\partial t}\,da + \oint_L \mathbf{T}\cdot d\mathbf{n}, \tag{2}$$

where L is the horizontal circuit surrounding the integrating volume; a and $\mathbf{n}$ are a coordinate on A and a vector normal to L, respectively; and $\mathbf{T} = \int_{-H}^{0} \mathbf{u}\,dz$. For example, if we take the mixed layer box between $\gamma^n = 27.4$ and 28.0 (Fig. 2), then A is the area GFF′G′ and L is the circuit B → C → C′ → B′ → B (or G → F → F′ → G′ → G, assuming the isopycnals in the mixed layer are almost vertical). The area integral can be performed in zonal and meridional directions;

$$\int_A da = \int dx \int_{Y_s(t)}^{Y_n(t)} dy, \tag{3}$$

where Y_n and Y_s are the meridional position of the isopycnals (CC′ and BB′), respectively. Using (3), (2) can be rewritten as

$$\int_{\mathrm{GFF'G'}} S\,da = \int_{\mathrm{C'}}^{\mathrm{C}} H_{n(t)}\upsilon_{n(t)}\,dx - \int_{\mathrm{B'}}^{\mathrm{B}} H_{s(t)}\upsilon_{s(t)}\,dx + \frac{\partial}{\partial t}\int_{\mathrm{GFF'G'}} H\,da + \oint_L \mathbf{T}\cdot d\mathbf{n}, \tag{4}$$

where $\upsilon_i = dY_i/dt$ $(i = n, s)$ is the velocity of the meridional migration of the isopycnals, and H_i, υ_i $(i = n, s)$ are evaluated on the isopycnals. The physical interpretation of these terms will be given in section 3c.

Since the inverse model attempts to estimate a mean state over decadal time scales, we average (4) in time. Denoting the time average by angle brackets,

$$\left\langle \int_{\mathrm{GFF'G'}} S\,da \right\rangle = \left\langle \int_{\mathrm{C'}}^{\mathrm{C}} H_{n(t)}\upsilon_{n(t)}\,dx \right\rangle - \left\langle \int_{\mathrm{B'}}^{\mathrm{B}} H_{s(t)}\upsilon_{s(t)}\,dx \right\rangle + \left\langle \oint_L \mathbf{T}\cdot d\mathbf{n} \right\rangle, \tag{5}$$

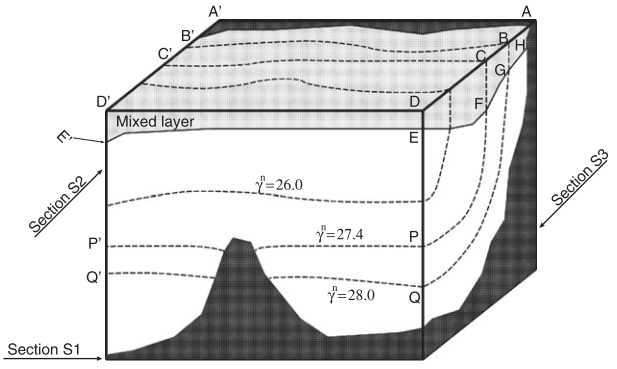

FIG. 2. Box inverse model with a surface layer box. This example box is surrounded by the Antarctic continent, two meridional hydrographic sections (sections S2 and S3), and one zonal hydrographic section (section S1). The isopycnals are shown by dashed lines. The isopycnal γ^n = 27.4 outcrops at points C and C′ and crosses the bottom of the mixed layer at F and F′. Similarly, the isopycnal γ^n = 28.0 outcrops at B and B′ and crosses the bottom of the mixed layer at G and G′. The mixed layer base on Section S2 (F′, G′, H′) are not visible on this schematic except for E′.

where we assumed trends in the volume of the mixed layer are negligible such that

$$\left\langle \frac{\partial}{\partial t}\int_{\mathrm{GFF'G'}} H\,da \right\rangle = 0.$$

By decomposing the last integral, we finally obtain

$$\left\langle \int_{\mathrm{GFF'G'}} S\,da \right\rangle = \left\langle \int_{\mathrm{C'}}^{\mathrm{C}} [H_{n(t)}\upsilon_{n(t)} + T_Y]\,dx \right\rangle - \left\langle \int_{\mathrm{B'}}^{\mathrm{B}} [H_{s(t)}\upsilon_{s(t)} + T_Y]\,dx \right\rangle + \left\langle \int_{\mathrm{B}}^{\mathrm{C}} T_X\,dy \right\rangle - \left\langle \int_{\mathrm{B'}}^{\mathrm{C'}} T_X\,dy \right\rangle, \tag{6}$$

where T_X, T_Y are the zonal and meridional components of the horizontal transport $\mathbf{T}$ in the mixed layer, respectively.

The volume conservation equation for an interior box corresponding to (6) is

$$\left\langle \int\int_{\mathrm{PP'Q'Q}} u_Y\,dz\,dx \right\rangle = \left\langle \int\int_{\mathrm{PFGQ}} u_X\,dz\,dy \right\rangle - \left\langle \int\int_{\mathrm{P'F'G'Q'}} u_X\,dz\,dy \right\rangle + \left\langle \int_{\mathrm{GFF'G'}} S\,da \right\rangle + \langle W_{\gamma^n=27.4}\rangle - \langle W_{\gamma^n=28.0}\rangle, \tag{7}$$

where (u_X, u_Y) are the zonal and meridional velocity, respectively, and $W_{\gamma^n=}$ is diapycnal volume flux across the isopycnal surface.

The constraint for the mixed layer inverse model is derived by adding (6) for all density layers that outcrop in the large basin

$$\left\langle \int_{\mathrm{HEE'H'}} S\,da \right\rangle = \left\langle \int_{\mathrm{D}}^{\mathrm{D'}} T_Y\,dx \right\rangle + \left\langle \int_{\mathrm{A}}^{\mathrm{D}} T_X\,dy \right\rangle - \left\langle \int_{\mathrm{A'}}^{\mathrm{D'}} T_X\,dy \right\rangle. \quad (8)$$

The inverse model not only determines the barotropic velocity corrections at the initial zero-velocity surfaces but also simultaneously determines the subduction (upwelling) fluxes from (into) the mixed layer box of the basin [lhs of (6)] as well as the diapycnal fluxes in the interior boxes ($W_{\gamma^n=}$) that satisfy (8) and interior conservation conditions such as (7). For the AABW box ($\gamma^n > 28.2$), the southern isopycnal AA′ is along the Antarctic continental boundary so that the second term on the rhs of (6) is zero {i.e., $\langle \int_{\mathrm{A'}}^{\mathrm{A}} [H_{s(t)} v_{s(t)} + T_Y]\,dx \rangle = 0$} hence, the first term is known. Proceeding northward, the transports across the isopycnals are estimated.

It is technically possible to add salt and temperature constraints to the mixed layer box similar to (8); however, surface fluxes have large uncertainties and addition of salt and temperature constraints did not improve the uncertainty of the solution. We also note that the freshwater flux into the surface layer is negligibly small [e.g., the average freshwater flux into the Pacific box $26.9 < \gamma^n < 27.0$ is 0.04 Sv based on the National Centers for Environmental Prediction (NCEP)–U.S. Department of Energy (DOE) reanalysis (Kanamitsu et al. 2002)], so the volume conservation can safely ignore the air–sea flux. In the interior boxes, however, salt and temperature (and silicate in the Indian Ocean, see the appendix) are conserved such that salt and temperature fluxes between the mixed layer box and interior boxes are determined to satisfy the interior conservation conditions.

b. Two hydrographic datasets

In this study, we have combined two hydrographic observation datasets: the first was obtained by the WHP between November 1987 and October 1998 and the second was obtained during revisits by the CLIVAR/Global Ocean Ship–based Hydrographic Investigation Program (GO-SHIP; Revisit) between August 2003 and May 2009 (Table 1). We assumed that the WHP and Revisit data were statistically independent. As discussed by Tziperman (1988), there are two possible ways to combine the datasets. We call the first method the direct method, as the ocean circulation is directly estimated by first averaging the two hydrographic datasets and then applying the inverse model to the averaged section data. We call the second method the merging method because the ocean circulation is estimated by applying the inverse model to the two hydrographic datasets separately and then averaging the resultant solutions.

In the direct method, the time variability, particularly the barotropic response to the wind, is expected to contribute most to the uncertainty (Ganachaud 2003), so it is not realistic to apply the same velocity correction to both WHP and Revisit data. Therefore, the conservation equation for the direct method applied to a box with two hydrographic sections is

$$\frac{1}{2}\sum_i (v_{ij}^{\mathrm{WA}} + b_i^{\mathrm{WA}}) + \frac{1}{2}\sum_i (v_{ij}^{\mathrm{RA}} + b_i^{\mathrm{RA}}) + \frac{1}{2}\sum_i (v_{ij}^{\mathrm{WB}} + b_i^{\mathrm{WB}}) + \frac{1}{2}\sum_i (v_{ij}^{\mathrm{RB}} + b_i^{\mathrm{RB}}) + W_{j-1} - W_j = 0, \quad (9)$$

where v_{ij}^{A} is the geostrophic shear calculated from the hydrographic data along section A at station i and depth j, b_i^{A} is the velocity correction along section A at station i on the assumed zero-velocity surface, W_j is the diapycnal volume flux across the surface at depth j, and superscripts W and R indicate the WHP and Revisit occupations, respectively. Ganachaud (2003) has confirmed that different hydrographic sections can be consistently combined as long as the time-mean Ekman transport is used for all sections. We use the Ekman transport averaged from August 1987 to July 2009 for the direct method calculated from NCEP–DOE reanalysis wind stress (Kanamitsu et al. 2002). The Ekman layer is assumed to have an exponential horizontal velocity profile with an e-folding scale of 60 m. We also constrained the upwelling transport between $\gamma^n = 26.2$ and $\gamma^n = 27.3$ by using estimates from Sallée et al. (2010), which we considered to be long-term averages.

For the merging method, we note that the best estimated mean of a quantity x_a with uncertainty $\pm\sigma_a$ and another quantity x_b with uncertainty $\pm\sigma_b$ is given by

$$\frac{x_a/\sigma_a^2 + x_b/\sigma_b^2}{1/\sigma_a^2 + 1/\sigma_b^2}$$

so that the combined uncertainty is

$$\frac{1}{\sqrt{1/\sigma_a^2 + 1/\sigma_b^2}}.$$

The Ekman transport was calculated separately for the WHP period (November 1987–October 1998) and Revisit period (August 2003–July 2009) and used in the respective inversions.

TABLE 3. Volume transport (Sv) estimates from the direct and merging inverse models.

	Section							
	P06	I3/4	I5	A10	SR1	I6S	I9S	SR3
Direct	19 ± 8	−10 ± 8	−12 ± 4	−5 ± 7	160 ± 6	170 ± 8	181 ± 7	176 ± 7
Merging	19 ± 8	−17 ± 7	−19 ± 7	−2 ± 7	157 ± 6	158 ± 7	178 ± 7	175 ± 7

Tziperman (1988) shows that these two estimates of the velocity correction and fluxes agree where the eddy transport across the hydrographic section is small. Although the zonal eddy transport across meridional hydrographic sections is not well known, there have been a few attempts to estimate the meridional eddy transport. The meridional component of eddy heat flux estimated from the satellite altimeter data (Fig. 1 of Wunsch 1999) suggests that the eddy heat flux is small near 30°S except for the western boundary of the South Atlantic Ocean. Indeed, estimates by the direct and merging methods (Table 3) generally agree with each other except in the Atlantic and Indian sectors where eddies are active.

c. *Velocity at 1000 dbar estimated by float drift*

Finally, the horizontal velocity across the hydrographic sections was constrained by the horizontal velocity estimated at 1000 dbar from subsurface float data. The float data consist of trajectory data from the WOCE subsurface floats (Davis 1998, 2005) and Argo floats (Lebedev et al. 2007). In the merging method, the WOCE data were used for the WHP inversion and the Argo data for the Revisit inversion. In the direct method, both data were combined before mapping. The WOCE data were downloaded from the WOCE Subsurface Float Data Assembly Center (http://wfdac.whoi.edu) and the Argo trajectory data are available online (YoMaHa07; http://apdrc.soest.hawaii.edu/projects/yomaha/). We used an objective mapping method of Davis (2005), where the mapped field are not only statistically optimal but also in perfect geostrophic balance (Fig. 1) and satisfy the no-normal-flow condition at the boundary. The number of trajectories is 67 649 from the WOCE subsurface floats and 638 171 from the Argo floats (Davis 2005; Katsumata and Yoshinari 2010). The application of the float constraints increased number of constraints applied to the model from 399 to 1628 [rank of the inversion matrix $\mathbf{E}$ in (A4) from 387 to 573]. Because, as discussed in section 2b, the eddy transport across the meridional sections crossing the Antarctic Circumpolar Current (ACC) is not known, we applied velocity constraints only across zonal sections (P6, I3/4, I5, and A10) by using the low-pass-filtered geostrophic pressure (Wijffels et al. 2001) with a cutoff length of 600 km. For the direct method inversion, 88% of the float constraints were satisfied within one standard deviation.

3. Results and discussion

a. *Isopycnal transports across hydrographic sections*

As previously noted, the only volume constraint imposed in the inverse model was the Pacific–Atlantic interbasin exchange via Bering Strait, other well-observed transports and interbasin exchanges (Drake Passage and Indonesian Throughflow) therefore can be used to assess the performance of the box inverse model (Table 3). Under the steady-state assumption, the southward transport across I3/4 (direct, 10 ± 8 Sv; merging, 17 ± 7 Sv) is equal to the Indonesian Throughflow transport (15 Sv) (Gordon et al. 2010). The transport across the meridional sections, the ACC transport, differed among the OGCMs: the average transport across Drake Passage (SR1, 68°W) was estimated to be 114 Sv (K7), 142 Sv [the OGCM for the Earth Simulator (OFES)], or 151 Sv [Simple Ocean Data Assimilation (SODA)]. The transports estimated by the inverse models (direct, 160 ± 6 Sv; merging, 157 ± 6 Sv) are slightly larger than but not inconsistent with recent estimates of 153 ± 5 Sv (Mazloff et al. 2010), 154 ± 38 Sv (Firing et al. 2011), and 152 Sv (Forget 2009), but notably larger than two observations made in January/February 2006 [Lowered Acoustic Doppler Current Profiler (LADCP)-referenced geostrophic transport, 136.6 ± 7 and 129 ± 7 Sv; LADCP-measured transport, 145 ± 8.8 and 137.9 ± 10.5 Sv] by Renault et al. (2011), who also discussed possible reasons for the differences in the transport estimates.

We also compared the horizontal water mass transports across hydrographic sections with outputs from the three OGCMs (Fig. 3, see Table 4 for detailed information about the OGCMs) and Sloyan and Rintoul (2001b) for common zonal sections. Across zonal sections (A10, I3/I4, I5, P6), the estimated transports are mostly consistent with the OGCMs within error bars. Lower Circumpolar Deep Water (i.e., LCDW) transport across P6 is northward and the OGCMs have smaller and either northward or southward transports. The OGCMs tended to overestimate the density of Lower Circumpolar

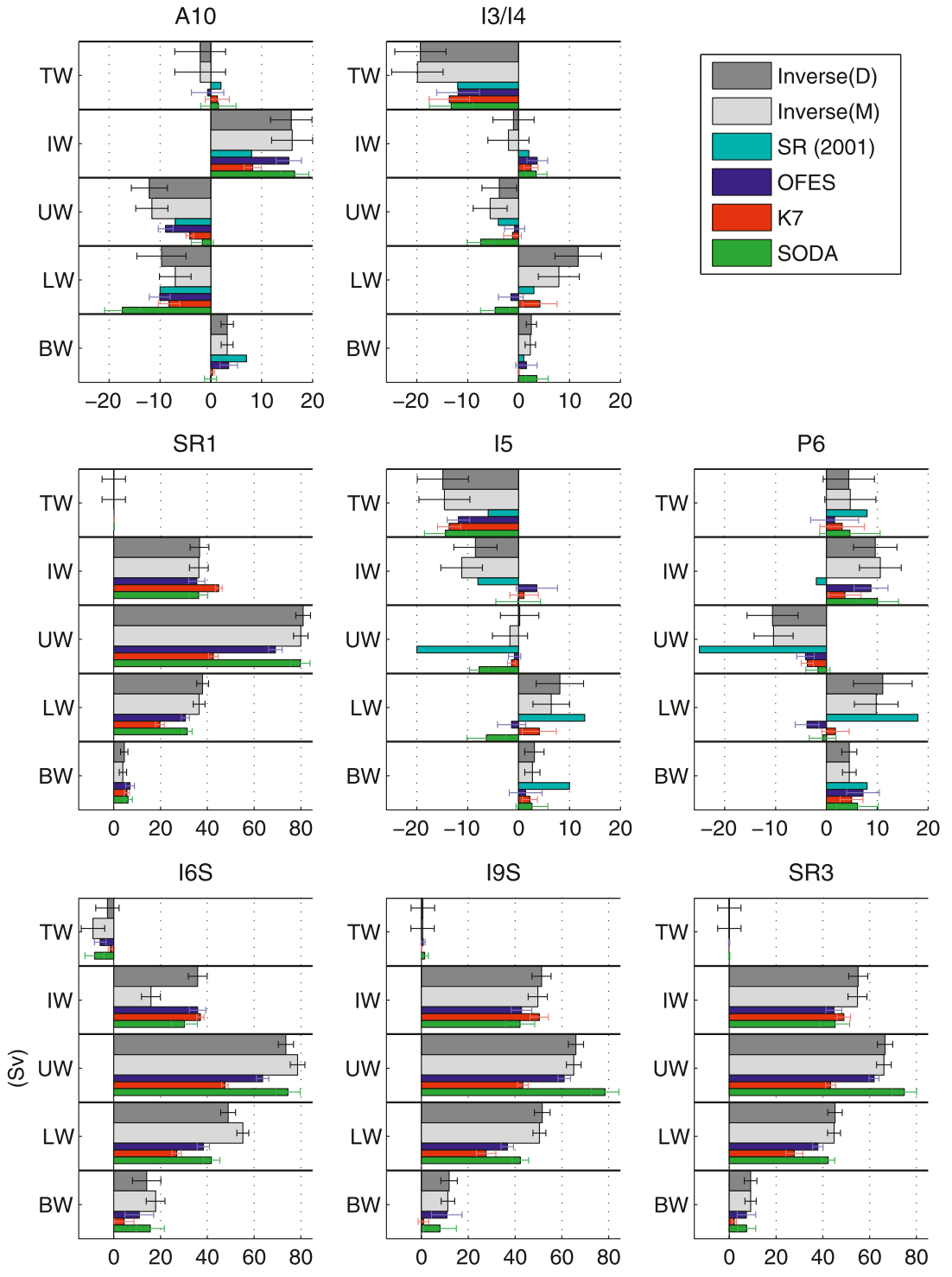

FIG. 3. Horizontal transport (Sv) across hydrographic sections. Gray bars show horizontal transport estimated by the present box inverse models (D, direct and M, merging); cyan bars show data from Sloyan and Rintoul (2001b); blue, red, and green bars show data from the OFES, K7, and SODA models, respectively. Model results are averaged over the period from 1980 to the end of the model integration time. Water masses are TW ($\gamma^n < 26.0$); IW ($26.0 < \gamma^n < 27.4$; 27.6 for the K7 model), UCDW (27.4(27.6) $\gamma^n < 28.0$), LCDW ($28.0 < \gamma^n < 28.2$); and BW ($28.2 < \gamma^n$). The black error bars show the uncertainties of the inverse estimates. The colored error bars show the standard deviations for the respective model transports under the assumption that each monthly-averaged transport is statistically independent.

TABLE 4. Numerical models where 20CRv2 = Twentieth-Century Reanalysis, version 2; KPP = *K*-profile parameterization; NCEP–NCAR = National Centers for Environmental Prediction–National Center for Atmospheric Research; SSS = sea surface salinity; SST = sea surface temperature; SSHA = sea surface height anomaly; *WOA* = *World Ocean Atlas*; and T = relaxation time. Version 2.2.4 of SODA is used (SODA 2.2.4).

	SODA 2.2.4	K7	OFES
Zonal grid size	0.4°*	1°	0.1°
Meridional	0.25°*	1°	0.1°
Levels	40	46	54
Period	1890–2008	1950–2009	1950–2010
Vertical mixing	KPP	Fickian and Noh Mixed-layer	KPP
Lateral mixing	Biharmonic	Gent–McWilliams	Biharmonic
Wind	20CRv2 (Compo et al. 2011)	Optimized NCEP–NCAR	NCEP–NCAR
Buoyancy	20CRv2 (Compo et al. 2011)	Optimized NCEP–NCAR	NCEP–NCAR bulk
SSS relaxation	T = 3 month (*WOA* 2001)	None	T = 6 days (*WOA* 1998)
South boundary relaxation	None (J. Carton 2011, personal communication)	70°–75°S, T = 30 days month^{-1} (*WOA* 1998)	72°–75°S, T = 1–720 days month^{-1} (*WOA* 1998)
Assimilation	Incremental Analysis Update	4D-VAR (adjoint)	None
Data	Temperature, salinity, SST	Temperature, salinity, SST, SSHA	None
Reference	Carton and Giese (2008), Carton et al. (2012)	Masuda et al. (2010)	Sasaki et al. (2008)

* Output is mapped onto a 0.5° × 0.5° grid.

Deep Water (not shown), and some of the transport estimated by the OGCMs attributed to BW might be LCDW. The inverse models have a southward transport of TW and IW at I3/I4 and I5, while the OGCMs generally have northward transport of IW and weaker southward transport of TW. The southward transport of TW across I5 might also have been overestimated by the box inverse model as unrealistically strong downwelling of 3 ± 5 Sv from TW to IW between I3/I4 and I5 (not shown) was estimated. Compared with the estimates of Sloyan and Rintoul (2001b), the present inverse models have a reduced deep circulation (Lower and Upper Circumpolar Deep Water) across P6 and I5 and suggest a closure of the deep cell by southward transport of thermocline and intermediate water masses in the Indian Ocean.

b. Mixed layer subduction/upwelling

The novel incorporation of the mixed layer box in the inverse model enables us to estimate the isopycnal subduction and upwelling into and from the interior ocean for each ocean basin and circumpolarly (Fig. 4). The subduction/upwelling estimates, direct and merging, were almost the same for the Pacific, Australia regions, and circumpolar total (Figs. 4c,d,e) but differed for the Atlantic and Indian sectors (Figs. 4a,b). As discussed by Tziperman (1988), the direct and merging results differ where eddies are active. The Atlantic region is bounded by two sections that cross rich eddy fields: the Agulhas retroflection south of Africa (I6S, 30°E) (section 7 of Lutjeharms 2006) and the Benguela Current (A10, 30°S) that transports Agulhas eddies into the South Atlantic. Indeed, Katsumata and Fukasawa (2011) in the revisit A10 section found a large eddy near 2°W that affected all density ranges with a recirculation transport of more than 40 Sv. The difference in the Indian region between the two methods most likely stems from the I5 section—the WHP and Revisit sections followed slightly different paths in the eastern half of the section over the Perth and South Australian Basins (not shown). The LCDW and BW differences in layer thickness and transport are ''correlated,'' and these difference are largely accounted for in the different subduction/upwelling transports between direct and merging.

Circumpolar total water mass subduction/upwelling estimates (Fig. 4e) are consistent between the two methods and clearly show the two-cell structure of the Southern Ocean meridional overturning circulation: Upper Circumpolar Deep Water ($27.4 < \gamma^n < 28.0$) upwells and diverges northward and southward to form the subducting Subantarctic Mode and Antarctic Intermediate Waters and Antarctic Bottom Water, respectively. A significant amount of the bottom water (direct, 8 ± 7 Sv; merging, 12 ± 5 Sv) is produced in the Atlantic sector, followed by the Indian sector (direct, 2 ± 7 Sv; merging, 2 ± 5 Sv upwelling) and the Pacific (direct, 0.4 ± 7 Sv; merging, 1 ± 5 Sv). Within the uncertainties, these estimates are consistent with the Antarctic Bottom Water (AABW) production rate estimated from the chlorofluorocarbon inventory (Orsi et al. 2002, who defined AABW as the water with $\gamma^n > 28.27$): 4.9 Sv in the Atlantic sector and 3.2 Sv in the Indian–Pacific sector.

The upwelling of UCDW has been recognized as a key component of the global meridional overturning

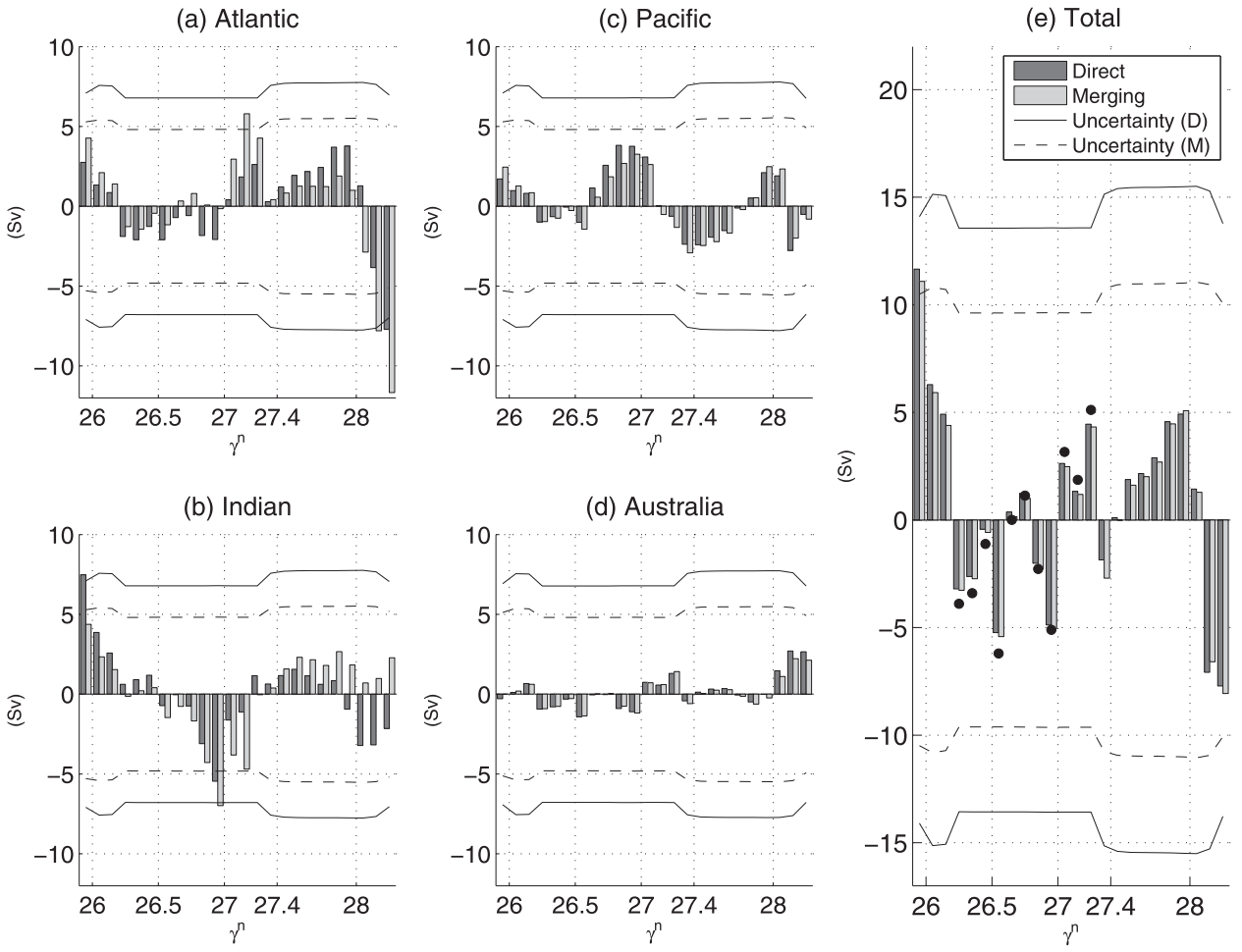

FIG. 4. Subduction/upwelling through the base of the Southern Ocean surface mixed layer. The bars show the subduction (negative)/upwelling (positive) estimated by the box inverse model (direct and merging). Black dots in (e) are the subduction/upwelling estimates by Sallée et al. (2010). Uncertainties (plus or minus one std dev) from the x axis are shown by the solid (for direct) and dashed (for merging) lines.

circulation (e.g., Sloyan and Rintoul 2001b; Marshall and Speer 2012). The upwelling is large in the Atlantic sector (direct, 15 ± 11 Sv; merging, 8 ± 8 Sv) and in the Indian sector (direct, 4 ± 11 Sv; merging, 12 ± 8 Sv). In the Australian and Pacific sectors, the UCDW is either only weakly upwelling (direct, 0.3 ± 10 Sv; merging, 0.4 ± 8 Sv) or subducting (direct, 4 ± 11 Sv; merging, 4 ± 8 Sv). The difference between the upwelling Atlantic and Indian sectors and the subducting Pacific sector is attributable to the upper part ($27.4 < \gamma^n < 27.7$) of UCDW (Figs. 4a–d). This density range is captured near the southern edge of the subduction/upwelling map (their Fig. 8) of Sallée et al. (2010), which shows subduction in the Pacific and upwelling in the Atlantic and Indian sectors. The upwelling is largely driven by the Ekman transport and the subduction is driven by southward eddy transports (see section 3c and Fig. 6).

Compared with the horizontal transports, the mixed layer transports in the Southern Ocean are much less constrained, with the result that uncertainties for subduction and upwelling are large (Fig. 4). Although the formal uncertainties are large, the actual error might be smaller because the constraints are much better satisfied than the formal a priori covariances (the appendix, section c). We note that the uncertainty estimates shown in Fig. 4 are based on the assumption that we have only two pieces of information regarding the diapycnal transports in this system: 1) mixed layer subduction/upwelling in the density range $26.2 < \gamma^n < 27.3$ based on estimates by Sallée et al. (2010), and 2) the magnitude of the diapycnal transport is about 10 Sv (the appendix, section b). The slight (~2 Sv) reduction of uncertainty in the density range $26.2 < \gamma^n < 27.3$ shows that the information 1) does not effectively constrain the subduction/upwelling. In the future, as observations accumulate and OGCMs are improved, it will be possible to prescribe each mean diapycnal transport in an inverse model such that we can solve for diapycnal transport anomalies from the expected

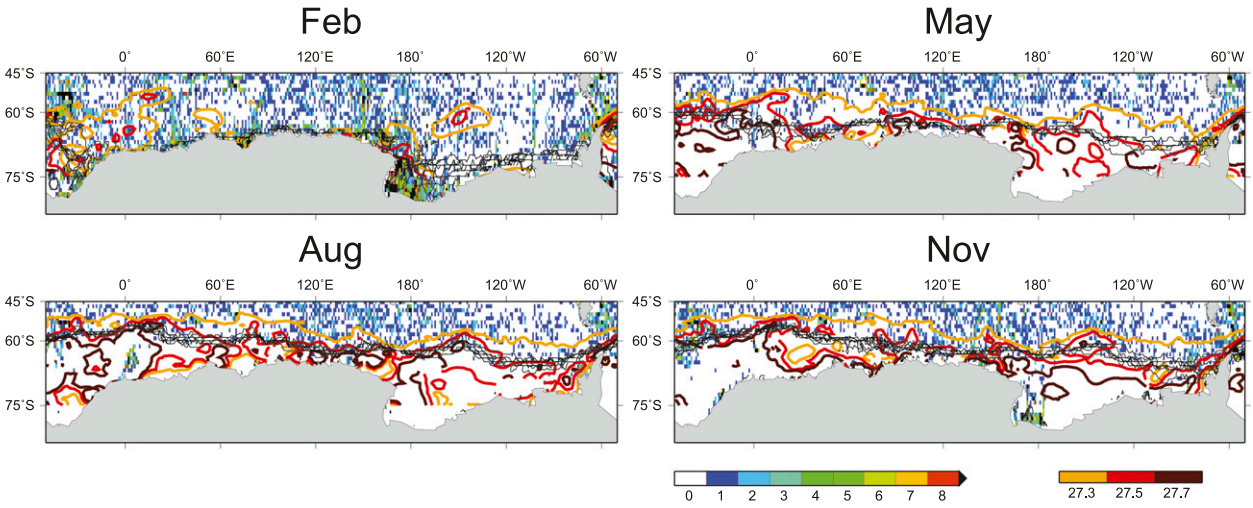

FIG. 5. Data density at the surface (color), ice edge (black lines), and surface isopycnals (thick contours). The number of surface salinity data were counted in the *World Ocean Database 2009* (Boyer et al. 2009) in a 1° by 1° grid and the number is shown by background color. Monthly ice concentration was calculated from daily data as the maximum concentration in the month. The daily sea ice concentration map was retrieved from the Advanced Microwave Scanning Radiometer for Earth Observing System (EOS) (AMSR-E) (Spreen et al. 2008). The black lines are the 90% sea ice concentration contours of the month from 2003 to 2010. The surface isopycnals were estimated from the CARS2009 temperature and salinity data (Ridgway et al. 2002). The left colorbar is for the salinity data density and the right colorbar is for the isopycnals.

mean with much reduced covariances R_{xx}, which will result in much reduced uncertainties. Given our current knowledge of the Southern Ocean circulation, however, we have to accept the uncertainties shown in Fig. 4.

c. *Diapycnal transport in the surface mixed layer*

1) EKMAN, GEOSTROPHIC, AND EDDY COMPONENTS

As shown, the inverse model (6) estimates the isopycnal subduction/upwelling transport between the mixed layer and interior ocean. From the estimated mixed layer transport we can calculate the meridional diapycnal fluxes in the surface mixed layer.

We note here that the constraints (6) are purely kinetic. More physical insights can be gained if we decompose the meridional transport T_Y into the Ekman transport T_{Ek} and horizontal transport in geostrophic flow T_G,

$$H_{n(t)}\upsilon_{n(t)} + T_Y = T_{\mathrm{Ek}} + T_G + T^*, \qquad (10)$$

where we define T^* as the residual. We note that the lhs of (10) was estimated by the inverse model. From the Commonwealth Scientific and Industrial Research Organisation (CSIRO) atlas of regional seas (CARS), hereafter CARS2009, climatological data (Ridgway et al. 2002), referenced to the absolute geostrophic pressure at 1000 dbar obtained from the Argo drift data (Katsumata and Yoshinari 2010), and the NCEP–DOE monthly reanalysis (Kanamitsu et al. 2002), we estimated the geostrophic transport T_G and Ekman transport T_{Ek} across isopycnal surfaces. Here, we assume that the residual in (10), T^*, represents "eddy" transport in the mixed layer. The location of the isopycnals as well as the depth of the mixed layer necessary for the calculation of T_G and T_{Ek} was determined from the CARS2009.

As the temporal resolution of our climatological data is monthly, we evaluate the time average as

$$\langle\cdot\rangle = \frac{1}{12}\sum_{m=1}^{12}\cdot,$$

where m is month. Accordingly the isopycnals used in (6) and (8) are the monthly mean isopycnals. The transport across these monthly mean isopycnals can give rise to a net diapycnal transport provided that it is followed by water mass modification owing to interior mixing or surface fluxes (Tandon and Garrett 1996). On the other hand, the monthly mean isopycnals can move without any horizontal movement of water masses if the water masses change densities by interior mixing or surface fluxes (Walin 1982). This latter effect is represented by the $H_i\upsilon_i$ ($i = n, s$) terms in (6).

Although CARS2009 provides monthly data as far south as the Antarctic continent, the Austral winter and early spring (June–September) data, particularly under seasonal ice, are extrapolated from summer data. The number of data under sea ice is very limited (Fig. 5). As the ice edge approximately coincides with the $\gamma^n = 27.5$

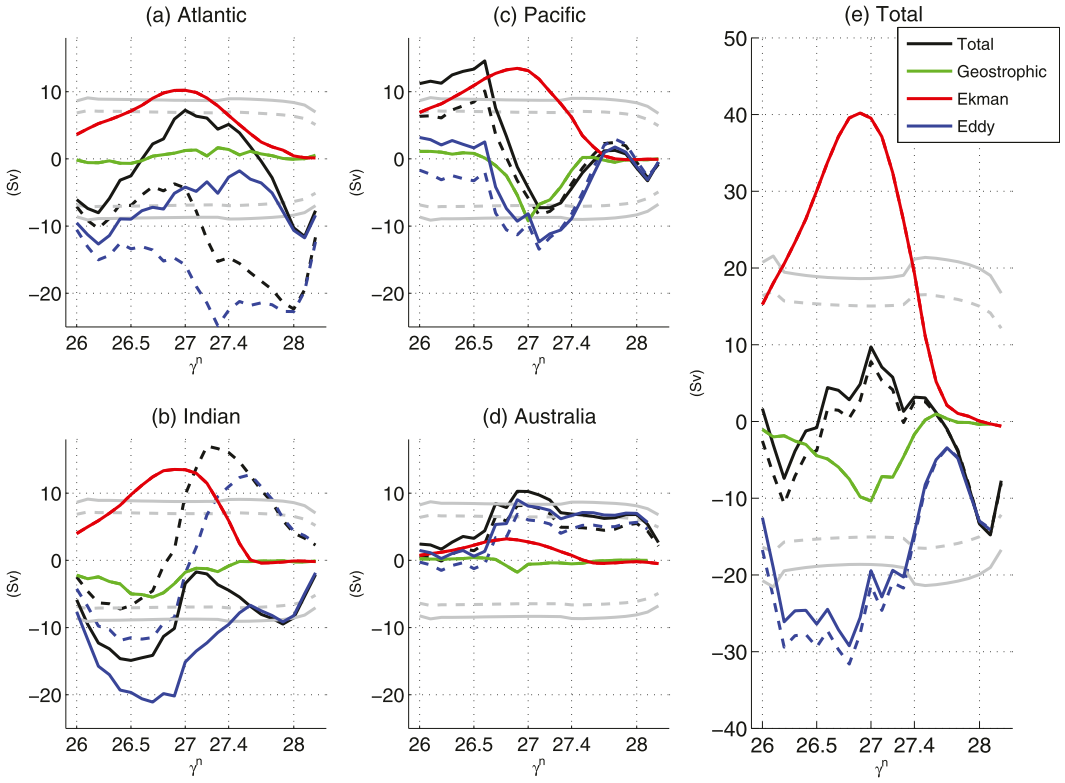

FIG. 6. Surface mixed layer meridional transport across isopycnals for Ekman (red), geostrophic (green), eddy (blue) and total (black, from inverse model). Positive is toward lighter density (i.e., northward). The gray lines show the uncertainties for the sum of the components from the horizontal axis provided by the inverse model. The solid lines show the direct estimates and dashed lines the merging estimates.

contour, the surface hydrographic data at the density range $\gamma^n > 27.5$ are probably not reliable.

The contribution from the $H_i v_i$ term appears large on monthly data. Between February and August, the $\gamma^n = 27.4$ contour, Fig. 5, shows a meridional displacement of roughly 20° latitudes or more, which translates to an average meridional speed of approximately $0.14\,\mathrm{m\,s^{-1}}$. On the other hand, an Ekman transport of 40 Sv spread over 20 000 km on a latitudinal circle and 60-m depth (thickness of the Ekman layer) is $0.03\,\mathrm{m\,s^{-1}}$. When averaged annually, however, the positive and negative contributions of the $H_i v_i$ terms tend to cancel each other. For example, if we assume $H \sim (1 - \cos \omega t)$ and $v \sim \sin \omega t$ (ω is the annual frequency with the time origin as February), $\langle Hv \rangle = 0$. By definition, the residual of $\langle H_i v_i \rangle$ is incorporated into the eddy component.

Figure 6 shows the surface mixed layer geostrophic, Ekman, and residual "eddy" components. Reflecting the difference in the direct and merging estimates of subduction/upwelling (Fig. 4), the total and eddy transports in the Atlantic and Indian sectors (Figs. 6a,b) differ between the direct and merging estimates, but the circumpolarly integrated estimates (Fig. 6e) are similar.

The diapycnal transports at $26.2 < \gamma^n < 27.3$ agree with Sallée et al. (2010): northward Ekman transport peak at $\gamma^n \approx \sigma_\theta = 26.9$, and southward eddy transport compensates for the Ekman transport (Fig. 6e). The difference in magnitude of each component between this study and previous studies can be attributed to different wind stress, hydrography, and geostrophic velocity data used in the calculation. Farther poleward at $27.3 < \gamma^n$, the Ekman transport decreases and becomes almost negligible at $27.6 < \gamma^n$, which agrees with the seasonal sea ice distribution (Fig. 5). In spite of the absence of the Ekman and geostrophic components, significant meridional transport exist at $27.6 < \gamma^n$, which is mostly under winter sea ice (Fig. 5). By definition (10), this southward transport is explained as by "eddies." Closer to the Antarctic coast, however, we note that the isopycnals deepen southward to support the Antarctic Slope Current (e.g., Rintoul and Bullister 1999), where a parameterization [see (11)] gives a northward eddy transport. We therefore speculate that the $H_i v_i (i = n, s)$ terms (i.e., water mass modification due to surface buoyancy flux and interior mixing) become important closer to the Antarctic coast ($27.6 < \gamma^n$).

2) MEAN EDDY DIFFUSIVITY

Although the uncertainties are large, the contrast between the strongest (almost 30 Sv in total) and the weakest (3 Sv) eddy transport is larger than the one standard deviation uncertainty. In an attempt to explain this difference, we calculated a mean eddy diffusivity. Following Treguier et al. (1997) and Sallée et al. (2011), geostrophic eddies resulting from baroclinic instability can be parameterized as

$$\langle u'h' \rangle = \kappa \left\langle \left. \frac{dz}{dy} \right|_{z=H} \right\rangle, \tag{11}$$

where the left-hand side is the cross-isopycnal eddy transport within the surface mixed layer box, κ is thickness diffusivity, and dz/dy is the slope of the isopycnal in the direction perpendicular to the isopycnal, evaluated at the bottom of the mixed layer ($z = H$).

By analogy, we can define a mean thickness diffusivity K as

$$\int_{B'}^{B} \langle T^* \rangle \, dl = K \int_{B'}^{B} \left\langle \left. \frac{dz}{dy} \right|_{z=H} \right\rangle dl. \tag{12}$$

The isopycnal slope was estimated from the CARS2009 climatology.

The mean diffusivity increases from about 2000 to 3000 $m^2 s^{-1}$ across the ACC between equivalent latitudes of 55° and 50°S (Fig. 7). This increase is similar to the latitudinal distribution of the diffusivity estimated by Sallée et al. (2011), using Lagrangian particle dispersion. Sallée et al. (2011) attributed this variability to the combination of changes in the eddy length scale and suppression of the length scale in the advecting mean flow (Ferrari and Nikurashin 2010). Our results, derived from hydrographic data, are thus consistent with the latitudinal variability of the eddy diffusivity within the ACC latitudes indicated by theoretical considerations.

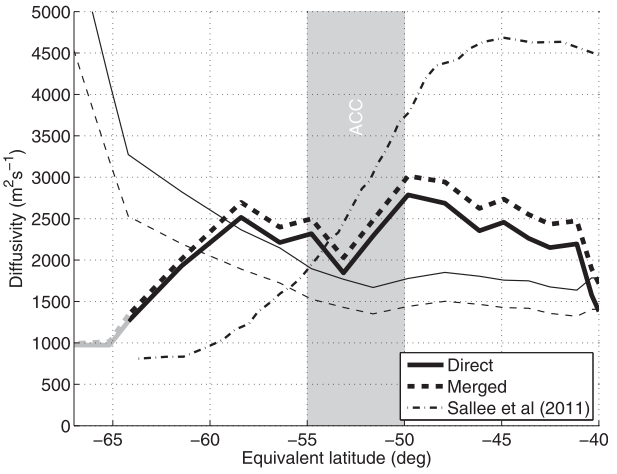

FIG. 7. Circumpolar mean surface mixed layer thickness diffusivity K ($m^2 s^{-1}$). The thick lines show the estimated diffusivity and the thin lines show the uncertainty from the x axis, under the assumption that no uncertainty is introduced by the climatological hydrography data. The gray lines south of 64°S are in the region covered by seasonal sea ice. The diffusivity was calculated as a function of the density and is plotted against the mean latitude of the isopycnals. The solid lines show for direct estimates and the dashed lines are for merging estimates. The vertical gray bar represents the mean position of the ACC. The dash–dot line shows the surface cross-stream eddy diffusion estimated by particle dispersion (Sallée et al. 2011).

d. Interior diapycnal transports

In theoretical treatments of the Southern Ocean meridional overturning circulation, it is often assumed that the interior diapycnal transport is negligible compared to the diapycnal transport within the surface mixed layer. The diapycnal transports estimated by the inverse model show that this is not the case for circumpolarly integrated transports (Fig. 8e). The interior diapycnal transport is toward lighter water at $26.1 < \gamma^n < 26.5$ and $27.2 < \gamma^n < 27.9$ and toward denser water for $26.5 < \gamma^n < 27.2$ and $27.9 < \gamma^n$. Breaking internal waves can explain the positive (upward) flux and the nonlinear effects in the equation of state (Klocker and McDougall 2010) can explain the negative (downward) transport. Indeed, the Klocker and McDougall (2010) estimates of the diapycnal transport owing to the nonlinearity in the equation of state are about 5 Sv at $\gamma^n \approx \omega = 27.4$ and approximately 10 Sv at $\gamma^n \approx \omega = 28.0$. The transport to denser water masses at $\gamma^n > 27.9$ may be explained by entrainment of slightly less dense water to denser Antarctic Bottom Water as dense shelf water flows down the continental slope. We note that the box inverse model only provides estimates of area-integrated quantities and the weak interior transport at $27.4 < \gamma^n < 27.8$ does not contradict the estimate of Klocker and McDougall (2010) because upwelling (mixing) of a similar magnitude can offset the downward diapycnal transport.

Although the diapycnal transports in the surface mixed layer and ocean interior are comparable when integrated circumpolarly (Fig. 8e), mixed layer diapycnal transport is generally larger than the interior diapycnal transport in the individual ocean basins (Figs. 8a–d). This means that the basin diapycnal transports within the surface mixed layer tend to cancel, but the interior diapycnal transports do not. Temporal variabilities in the mixed layer across the meridional sections (I6S, I9S, SR1, SR3; see Table 1) can explain the large surface diapycnal transport estimated using (6), as these variabilities cancel out when integrated circumpolarly.

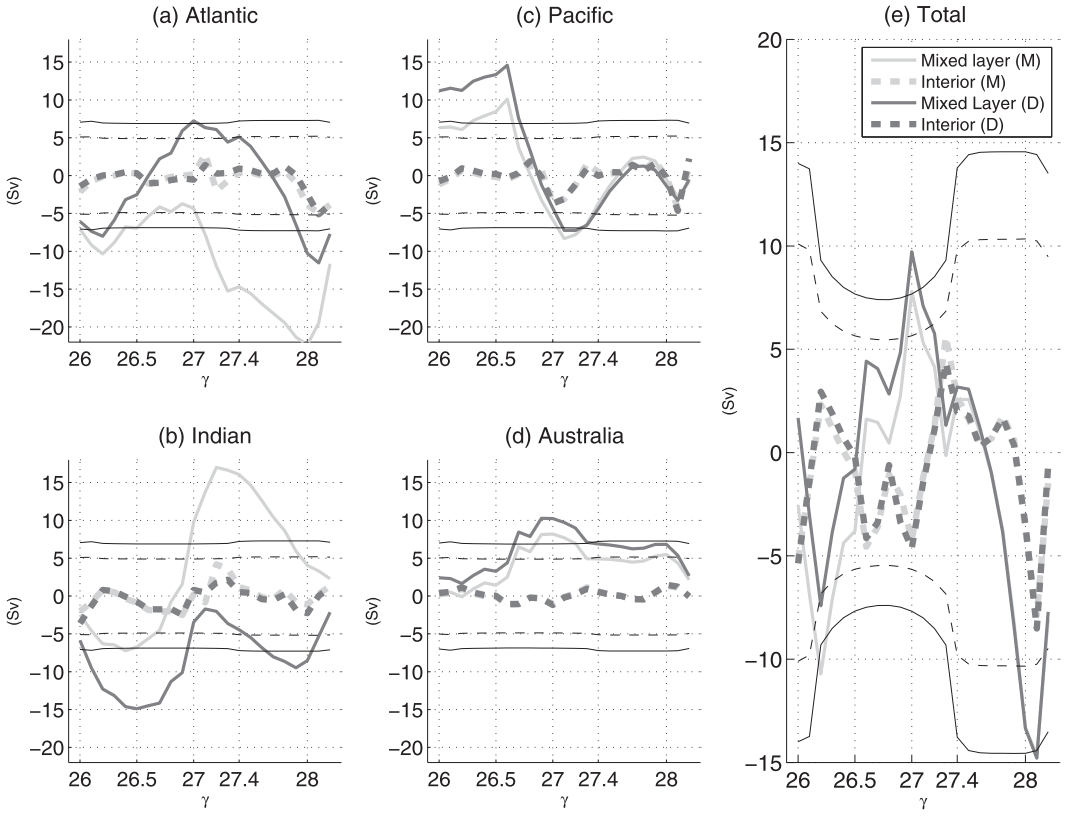

FIG. 8. Comparison of mixed layer diapycnal transport (thick solid, same as the black lines in Fig. 6) and interior ocean (i.e., below the mixed layer) diapycnal transport (thick dashed). The uncertainties from the horizontal axis are shown for the interior diapycnal transport for direct (dark gray) and merging (light gray) inverse models. Positive is toward lighter densities.

The diapycnal transports estimated by the box inverse model are largely consistent with the results of an ice–ocean coupled model (Iudicone et al. 2008a). In the surface mixed layer, which Iudicone et al. (2008a) called a ''bowl,'' the ice–ocean coupled model showed mode waters losing buoyancy for $\gamma^n < 26.8$, buoyancy gain for $26.8 < \gamma^n < 28.0$, and buoyancy loss for $28.0 < \gamma^n$. Considering the coupled model's tendency to overestimate the density of the intermediate waters, and the large uncertainties in our estimate, the agreement between the studies seems reasonable. The analysis of Iudicone et al. (2008a) showed that buoyancy gain at $26.8 < \gamma^n < 28.0$ results from a surface buoyancy flux and opposite mixing by eddies. Also the density gain at $28.0 < \gamma^n$ is mainly explained by surface forcing and eddy fluxes. The agreement of the interior mixing between the box inverse model and the coupled model is not as good; the coupled model predicts two density-gaining flux peaks at $\gamma^n \approx 27.6$ and $\gamma^n \approx 28.1$ (Iudicone et al. 2008a), whereas the box inverse model peaks are at $\gamma^n \approx 26.6$, 27.0, and 28.1 (Fig. 8e).

We attempted to estimate a mean interior diapycnal diffusivity similar to (12), but the estimates are found very sensitive to assumed density structure of the upwelling/subduction transport, which is not known accurately from the hydrographic observations, particularly under the ice ($\gamma^n > 27.6$) where the large diapycnal transports are found. At this density range, the large density-gaining flux, both in the mixed layer and in the interior (Fig. 8), emphasizes the importance of data collection efforts under sea ice (e.g., Charrassin et al. 2008).

4. Conclusions

We have examined two different methods to combine data from the two occupations of eight hydrographic sections (Fig. 1) and the middepth velocity estimated from float drift data for estimation of the Southern Ocean circulation; interior isopycnal, mixed layer subduction/upwelling, and interior ocean diapycnal transports. Reflecting the paucity of data, the estimated subduction/upwelling across the base of the mixed layer and interior ocean were accompanied by uncertainties of similar magnitude to that of the transports themselves. Use of the

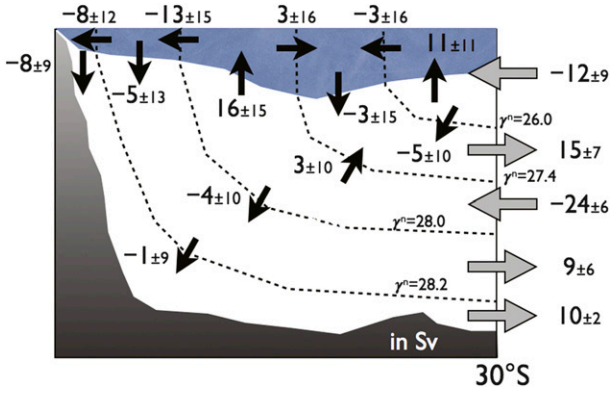

FIG. 9. Summary of the Southern Ocean circulation including isopycnal interior transport, subduction, and upwelling (Sv) across the base of the mixed layer and, diapycnal transport in the mixed layer and interior ocean. Solution shown is for the merging inverse model.

merging method, in which two inverse solution sets were averaged for combining the data from the two occupations, resulted in lower uncertainties than the direct method, in which the two sets of hydrographic data were averaged before inversion.

The estimated meridional overturning circulation is summarized in Fig. 9. The estimated upwelling/subduction at the base of the mixed layer is consistent with the general picture of the Southern Ocean meridional overturning circulation obtained by previous studies. The Upper Circumpolar Deep Water ($27.4 < \gamma^n < 28.0$) upwelling of 16 ± 15 Sv estimated by the merging method (17 ± 21 Sv by the direct method) reaches the surface and diverges equatorward and poleward. The equatorward branch transports 3 ± 16 Sv (3 ± 21 Sv) of Subantarctic Mode and Antarctic Intermediate Water ($26.0 < \gamma^n < 27.4$). On the continental shelves around Antarctica, the upwelling UCDW increases in density to become 5 ± 13 Sv (6 ± 18 Sv) of Lower Circumpolar Deep Water ($28.0 < \gamma^n < 28.2$) and 8 ± 9 Sv (8 ± 13 Sv) of Antarctic Bottom Water ($28.2 < \gamma^n$).

We have provided an indirect estimate of diapycnal transports, including the density range under sea ice in wintertime (mostly $\gamma^n > 27.5$). The meridional diapycnal transport in the mixed layer is largely southward and largest at $\gamma^n \approx 26.7$ and decreases poleward; this decrease can be explained by a poleward decrease in eddy diffusivity, which is consistent with cross-isopycnal eddy diffusion estimated from particle dispersion experiments (Sallée et al. 2011).

A novel aspect of the inverse model is the explicit separation of the surface mixed layer from the interior ocean. This has shown that interior diapycnal transports—buoyancy loss or gain—are comparable in magnitude to the horizontal diapycnal transports within the surface mixed layer. Resolution of both interior ocean mixing and mixed layer dynamics is vital for accurate representation of the Southern Ocean overturning circulation.

The southward transport under ice and significant interior diapycnal transports have been simulated in numerical models (e.g., Iudicone et al. 2008a; Urakawa and Hasumi 2012) but have never been observed. The box inverse model shows that these simulations are consistent with the observed hydrographic data; however, results from the box inverse model are accompanied with large uncertainties. Increased high-latitude observations, particularly in austral winter, will result in a more reliable quantitative description of ocean circulation from both inverse box models and sophisticated assimilation models [e.g., four-dimensional variational data assimilation (4D-VAR) methods]. Accurate uncertainties estimated by these models would be of great use, too.

Acknowledgments. The hydrographic data were collected as contribution to World Ocean Circulation Experiment and GO-SHIP (www.go-ship.org). We appreciate the efforts of all scientific and ship personnel who enabled collection of the data. The Argo data were collected and made freely available by the International Argo Project and associated contributing national programs (http://www.argo.ucsd.edu, http://argo.jcommops.org). Argo is a pilot program of the Global Ocean Observing System. The CARS2009 data were obtained through the CSIRO Marine Laboratories. NCEP Reanalysis 2 data were provided by the NOAA/OAR/ESRL PSD, Boulder, Colorado, from its website (http://www.esrl.noaa.gov/psd). The OFES data were made available by Dr. H. Sasaki, the Earth Simulator Center, JAMSTEC. The data for subduction/upwelling constraints ($26.2 < \gamma^n < 27.3$) as well as diffusivity for Fig. 7 were provided by courtesy of Dr. Sallée. BMS was supported by the Australian Climate Change Science Program, funded jointly by the Department of Climate Change and Energy Efficiency and CSIRO.

APPENDIX

Box Inverse Model

Column and row scalings are vital for realistic inverse modeling (McIntosh and Rintoul 1997). The column scaling expresses the a priori knowledge about the magnitude of the solution vector and the row scaling measures our confidence in each constraint.

a. Constraints

The a priori covariances for model equations used in the row scaling were fixed following Ganachaud et al.

(2000) and Ganachaud (2003). For horizontal transport across hydrographic sections, time variability dominates other uncertainties such as internal tides, ageostrophic flows, and treatment of the bottom data on slopes. Applying Table 2 of Ganachaud (2003) conservatively, we assign a priori covariances of $(5.0\,\mathrm{Sv})^2$, $(4.0\,\mathrm{Sv})^2$, $(3.0\,\mathrm{Sv})^2$, $(2.0\,\mathrm{Sv})^2$, and $(1.0\,\mathrm{Sv})^2$, for Thermocline Water, Intermediate Water, Upper Circumpolar Deep Water, Lower Circumpolar Deep Water, and Bottom Water, respectively.

In addition to this time variability, uncertainties due to internal waves [$(3\,\mathrm{Sv})^2$ for $\gamma^n < 27.4$], ageostrophic flows [$(2\,\mathrm{Sv})^2$], and the bottom triangle [$(2\,\mathrm{Sv})^2$] are added. These uncertainties resulted in large barotropic transport uncertainties for the integrated water column. We therefore placed an additional covariance on barotropic transport conservation equation of $(6\,\mathrm{Sv})^2$.

Sallée et al. (2010) estimated the subduction from and upwelling into the Southern Ocean surface mixed layer in the density range $26.2 < \gamma^n < 27.3$. We used their estimates to constrain the subduction/upwelling between the surface boxes and the interior boxes with an a priori uncertainty of $(5\,\mathrm{Sv})^2$. Subduction and upwelling of densities heavier than 27.3 were not constrained. The South Indian box between I3/4 (20°S) and I5 (34°S) does not have a surface box and outcropping layers there receive a volume flux from heat and freshwater forcing estimated by using the NCEP–DOE reanalysis (Kanamitsu et al. 2002). The uncertainty of Thermocline Water conservation is also applied to the volume budget of the surface boxes. The volume budget variances calculated using these a priori covariances are of the same order as the temporal variances of the volume budget calculated by the K7 model. In fact, the inverse transport estimates are not very sensitive to the choice of the a priori covariances. We tested the sensitivity of the box inverse model by using the temporal variances from the K7 model as a priori covariances. The difference in transport from the standard case (Table 3) was no greater than 3 Sv and was mostly less than 1 Sv.

Several deep closed basins, forming cul-de-sacs, are found in the subtropical zonal sections: in the Tasman Sea in the South Pacific Ocean (P6); in the Mozambique, Mascarene, Crozet, and Central Indian Basins and Natal Valley in the Indian Ocean (I3, I5); and in the Namibia Abyssal Plain in the Atlantic (A10). Deep ocean transport into these basins was constrained to be 0 ± 2 Sv. The following well-observed deep flows were constrained; BW and LCDW through the Tonga–Kermadec Trench, 6 ± 1 and 9 ± 1 Sv, respectively (Whitworth et al. 1999); and BW through the Brazil Basin, 4 ± 2 Sv (Speer and Zenk 1993). Finally, interbasin transport from the Pacific to the Atlantic, via Bering Strait, was constrained at 0.8 ± 0.3 Sv (Roach et al. 1995).

A priori covariances for potential temperature and salinity were fixed following the estimate suggested by Ganachaud et al. (2000). The sample averages were subtracted from the potential temperature and salinity. Ganachaud et al. (2000) assumed that most of the covariances of these tracers derived from the covariances of the transport (rather than from changes in the tracer concentration) and evaluated the covariances as

$$\langle n_c^2 \rangle = 4 \times \langle n_M^2 \rangle \times \langle \Delta C^2 \rangle , \tag{A1}$$

where the factor 4 accounts for the possible correlation between the average and the horizontal "eddy" component. We used $\langle \Delta C^2 \rangle = (4.0^\circ\mathrm{C})^2$ and $\langle \Delta C^2 \rangle = (0.5\,\mathrm{g\,kg^{-1}})^2$ for temperature and salinity, respectively. In the South Indian Ocean box between I3/4 and I5, vertically integrated silicate is conserved up to $100\,\mathrm{kmol\,Si\,s^{-1}}$ (Ganachaud 2003).

We note here that the covariance matrix $\mathbf{R}_{nn}$ is not diagonal. In a unit time, the volume of a box defined by two hydrographic sections, (here, denoted by superscripts A and B) and two isopycnals (j and $j + 1$) changes by

$$\Delta V_j = v_j^A - v_j^B + W_j - W_{j+1} , \tag{A2}$$

where v^A and v^B are volume fluxes through the hydrographic sections, and W_j and W_{j+1} are the diapycnal fluxes. By construction, the first off-diagonal component of $\mathbf{R}_{nn}$ is

$$\langle \Delta V_j \Delta V_{j+1} \rangle = -\langle W_{j+1}^2 \rangle . \tag{A3}$$

Hence, assuming all $\langle W_j^2 \rangle = \sigma_w^2$ (constant), the diagonal component (k, k) of $\mathbf{R}_{nn}$ is $\langle v_{Ak}^2 \rangle + \langle v_{Bk}^2 \rangle + 2\sigma_w^2$, whereas the off-diagonal components $(k, k + 1)$ and $(k + 1, k)$ are $-\sigma_w^2$.

The covariances for the float velocity constraint use the uncertainties estimated in the mapping by Katsumata and Yoshinari (2010), which includes observational and mapping errors as well as eddy covariances.

b. Solution covariances

Our a priori knowledge of the solution vector is expressed in the solution covariances. The solution vector consists of the barotropic velocity correction b_i at the zero velocity surfaces and diapycnal fluxes W_j of volume, temperature, and salinity. Long-term mooring data suggest that the temporal variability of deep horizontal currents is on the order of centimeters per second (Whitworth et al. 1999). Diapycnal fluxes are difficult to measure directly but previous observational data (e.g., Sloyan and Rintoul 2001b; Ganachaud and

Wunsch 2000) and numerical models (e.g., Iudicone et al. 2008a) suggest values on the order of 1 to 10 Sv. After some trials, we chose $(10^{-2}\,\mathrm{m\,s^{-1}})^2$ as the covariance of the barotropic velocity correction and $(10\,\mathrm{Sv})^2$ as the covariance of the diapycnal fluxes.

Mathematically, the inverse problem estimates the solution vector $\mathbf{x}$, that minimizes the cost function

$$J = (\mathbf{y} - \mathbf{E}\mathbf{x})^{\mathrm{T}}\mathbf{R}_{nn}^{-1}(\mathbf{y} - \mathbf{E}\mathbf{x}) + \mathbf{x}^{\mathrm{T}}\mathbf{R}_{xx}^{-1}\mathbf{x}, \qquad \text{(A4)}$$

where the matrix $\mathbf{E}$ and the vector $\mathbf{y}$ are constructed model equations [e.g., (9)]. Under the Gauss–Markov interpretation of the inverse problem (Wunsch 2006), the row and column scalings are expressed as the matrices $\mathbf{R}_{nn}$ and $\mathbf{R}_{xx}$, respectively. We examined our choice of $\mathbf{R}_{nn}$ and $\mathbf{R}_{xx}$ using the L-curve method (Hansen 1992), where a plot of the first term versus the second term on the rhs of (A4) yields an L-shaped curve. At the corner of the L, there is a good balance between the two terms. Our choice of $\mathbf{R}_{nn}$ and $\mathbf{R}_{xx}$ is near the corner and also gives a realistic Indonesian Throughflow transport.

c. Diagnosis

As noted by Macdonald et al. (2009), the constraints are better met than would be expected if the errors have an independent Gaussian distribution. In the direct method, of the 399 constraints which do not involve float velocity, only one constraint was not within 3σ (with σ being the a priori standard uncertainty) and seven were not within 1σ. If the error distribution was perfectly Gaussian, the values should be 1 and 126, respectively. The constraints not met were cul-de-sac closures (in the deep Tasman Sea across P6, bottom water transport across P6, the Natal Valley and the Crozet Basin across I5, and the Mascarene Basin across I3). The temperature transport results (not shown) are largely consistent with past estimates (e.g., Macdonald and Wunsch 1996; Ganachaud and Wunsch 2000; Sloyan and Rintoul 2001b; Lumpkin and Speer 2007).

d. Sensitivity

Since a surface mixed layer box is introduced in this work, sensitivity of the solution to the mixed layer configuration was examined by varying the mixed layer depth by ±50% of the original depth defined in section 2a. The solutions are found not overly sensitive to the choice of the mixed layer depth; the ±50% variation resulted in the differences in the subduction/upwelling transport of less than 1 Sv except for the top two layers in the Pacific box (which showed 2.3 and 1.2 Sv changes). The horizontal transport within the mixed layer varied almost linearly with the mixed layer depth, but the total isopycnal transport varied less than 1 Sv.

REFERENCES

Boyer, T. P., and Coauthors, 2009: *World Ocean Database 2009.* Government Printing Office, 216 pp.

Carton, J. A., and B. S. Giese, 2008: A reanalysis of ocean climate using Simple Ocean Data Assimilation (SODA). *Mon. Wea. Rev.,* **136,** 2999–3017.

Cerovečki, I., L. D. Talley, and M. R. Mazloff, 2011: A comparison of Southern Ocean air–sea buoyancy flux from an ocean state estimate with five other products. *J. Climate,* **24,** 6283–6306.

Charrassin, J. B., and Coauthors, 2008: Southern Ocean frontal structure and sea-ice formation rates revealed by elephant seals. *Proc. Natl. Acad. Sci. USA,* **105,** 11 634–11 639.

Compo, G. P., and Coauthors, 2011: The twentieth-century reanalysis project. *Quart. J. Roy. Meteor. Soc.,* **137,** 1–28.

Davis, R. E., 1998: Preliminary results from directly measuring middepth circulation in the tropical and South Pacific. *J. Geophys. Res.,* **103** (C11), 24 619–24 639.

——, 2005: Intermediate-depth circulation of the Indian and South Pacific Oceans measured by autonomous floats. *J. Phys. Oceanogr.,* **35,** 683–707.

Dong, S., J. Sprintall, S. T. Gille, and L. Talley, 2008: Southern Ocean mixed-layer depth from Argo float profiles. *J. Geophys. Res.,* **113,** C06013, doi:10.1029/2006JC004051.

Ferrari, R., and M. Nikurashin, 2010: Suppression of eddy diffusivity across jets in the Southern Ocean. *J. Phys. Oceanogr.,* **40,** 1501–1519.

Firing, Y. L., T. K. Chereskin, and M. R. Mazloff, 2011: Vertical structure and transport of the Antarctic Circumpolar Current in Drake Passage from direct velocity observations. *J. Geophys. Res.,* **116,** C08015, doi:10.1029/2011JC006999.

Forget, G., 2009: Mapping ocean observations in a dynamical framework: A 2004–06 ocean atlas. *J. Phys. Oceanogr.,* **40,** 1201–1221.

Ganachaud, A., 2003: Error budget of inverse box models: The North Atlantic. *J. Atmos. Oceanic Technol.,* **20,** 1641–1655.

——, and C. Wunsch, 2000: Improved estimates of global ocean circulation, heat transport and mixing from hydrographic data. *Nature,* **408,** 453–457.

——, ——, J. Marotzke, and J. Toole, 2000: Meridional overturning and large-scale circulation of the Indian Ocean. *J. Geophys. Res.,* **105,** 26 117–26 134.

Gordon, A. L., and Coauthors, 2010: The Indonesian throughflow during 2004–2006 as observed by the INSTANT program. *Dyn. Atmos. Oceans,* **50,** 115–128.

Hallberg, R., and A. Gnanadesikan, 2006: The role of eddies in determining the structure and response of the wind-driven Southern Hemisphere overturning: Results from the Modeling Eddies in the Southern Ocean (MESO) project. *J. Phys. Oceanogr.,* **36,** 2232–2252.

Hansen, P. C., 1992: Analysis of discrete ill-posed problems by means of the L-Curve. *SIAM Rev.,* **34,** 561–580.

Hernández-Guerra, A., T. M. Joyce, E. Fraile-Nuez, and P. Vélez-Belchí, 2010: Using Argo data to investigate the meridional overturning circulation in the North Atlantic. *Deep-Sea Res. I,* **57,** 29–36.

Intergovernmental Oceanographic Commission, 2010: The international thermodynamic equation of seawater—2010: Calculation and use of thermodynamic properties. UNESCO Intergovernmental Oceanographic Commission Manuals and Guides 56, 196 pp.

Iudicone, D., G. Madec, B. Blanke, and S. Speich, 2008a: The role of Southern Ocean surface forcings and mixing in the global conveyor. *J. Phys. Oceanogr.,* **38,** 1377–1400.

——, S. Speich, G. Madec, and B. Blanke, 2008b: The global conveyor belt from a Southern Ocean perspective. *J. Phys. Oceanogr.,* **38,** 1401–1425.

Jackett, D. R., and T. J. McDougall, 1997: A neutral density variable for the world's oceans. *J. Phys. Oceanogr.,* **27,** 237–263.

Jacobs, S. S., 2004: Bottom water production and its links with the thermohaline circulation. *Antarct. Sci.,* **16,** 427–437.

Johnson, G. C., S. Mecking, B. M. Sloyan, and S. E. Wijffels, 2007: Recent bottom-water warming in the Pacific Ocean. *J. Climate,* **20,** 5365–5375.

Kanamitsu, M., W. Ebisuzaki, J. Woollen, S. Yang, J. J. Hnilo, M. Fiorino, and G. L. Potter, 2002: NCEPDOE AMIP-II Reanalysis (R-2). *Bull. Amer. Meteor. Soc.,* **83,** 1631–1643.

Katsumata, K., and H. Yoshinari, 2010: Uncertainties in global mapping of Argo drift data at the parking level. *J. Oceanogr.,* **66,** 553–569.

——, and M. Fukasawa, 2011: Changes in meridional fluxes and water properties in the Southern Hemisphere subtropical oceans between 1992/1995 and 2003/2004. *Prog. Oceanogr.,* **89,** 61–91.

Klocker, A., and T. J. McDougall, 2010: Influence of the nonlinear equation of state on global estimates of dianeutral advection and diffusion. *J. Phys. Oceanogr.,* **40,** 1690–1709.

Kuhlbrodt, T., A. Griesel, M. Montoya, A. Levermann, M. Hofmann, and S. Rahmstorf, 2007: On the driving processes of the Atlantic meridional overturning circulation. *Rev. Geophys.,* **45,** RG2001, doi:10.1029/2004RG000166

Lebedev, K., H. Yoshinari, N. A. Maximenko, and P. W. Hacker, 2007: YoMaHa'07: Velocity data assessed from trajectories of Argo floats at parking level and at the sea surface. IPRC Tech. Note 4 (2), 20 pp.

Lumpkin, R., and K. Speer, 2007: Global ocean meridional overturning. *J. Phys. Oceanogr.,* **37,** 2550–2562.

Lutjeharms, J. R. E., 2006: *The Agulhas Current.* Springer, 329 pp.

Macdonald, A. M., and C. Wunsch, 1996: An estimate of global ocean circulation and heat fluxes. *Nature,* **382,** 436–439.

——, S. Mecking, P. E. Robbins, J. M. Toole, G. C. Johnson, L. Talley, M. Cook, and S. E. Wijffels, 2009: The WOCE-era 3-D Pacific Ocean circulation and heat budget. *Prog. Oceanogr.,* **82,** 281–325.

Marshall, J., and T. Radko, 2003: Residual-mean solutions for the Antarctic Circumpolar Current and its associated overturning circulation. *J. Phys. Oceanogr.,* **33,** 2341–2354.

——, and K. Speer, 2012: Closure of the meridional overturning circulation through Southern Ocean upwelling. *Nat. Geosci.,* **5,** 171–180.

Masuda, S., and Coauthors, 2010: Simulated rapid warming of abyssal North Pacific waters. *Science,* **329,** 319–322.

Mazloff, M. R., P. Heimbach, and C. Wunsch, 2010: An eddy-permitting Southern Ocean State Estimate. *J. Phys. Oceanogr.,* **40,** 880–899.

McCartney, M. S., and K. A. Donohue, 2007: A deep cyclonic gyre in the Australian–Antarctic Basin. *Prog. Oceanogr.,* **75,** 675–750.

McDonagh, E. L., 2009: RRS James Cook Cruise JC031, 03 Feb-03 Mar 2009. Hydrographic sections of Drake Passage. National Oceanography Centre Southampton Tech. Rep., 170 pp.

McIntosh, P. C., and S. R. Rintoul, 1997: Do box inverse models work? *J. Phys. Oceanogr.,* **27,** 291–308.

Naveira Garabato, A. C., K. L. Polzin, B. A. King, K. J. Heywood, and M. Visbeck, 2004: Widespread Intense turbulent mixing in the Southern Ocean. *Science,* **303,** 210–213.

——, D. P. Stevens, A. J. Watson, and W. Roether, 2007: Short-circuiting of the overturning circulation in the Antarctic Circumpolar Current. *Nature,* **447,** 194–197.

Olbers, D., and M. Visbeck, 2005: A model of the zonally averaged stratification and overturning in the Southern Ocean. *J. Phys. Oceanogr.,* **35,** 1190–1205.

Orsi, A. H., W. M. Smethie, and J. L. Bullister, 2002: On the total input of Antarctic waters to the deep ocean: A preliminary estimate from chlorofluorocarbon measurements. *J. Geophys. Res.,* **107,** 3122, doi:10.1029/2001JC000976.

Renault, A., C. Provost, N. Sennéchael, and A. Kartavtseff, 2011: Two full-depth velocity sections in the Drake Passage in 2006: Transport estimates. *Deep-Sea Res. II,* **58,** 2572–2591.

Ridgway, K. R., J. R. Dunn, and J. L. Wilkin, 2002: Ocean interpolation by four-dimensional weighted least squares: Application to the waters around Australasia. *J. Atmos. Oceanic Technol.,* **19,** 1357–1375.

Rintoul, S. R., and J. L. Bullister, 1999: A late winter hydrographic section from Tasmania to Antarctica. *Deep-Sea Res. I,* **46,** 1417–1454.

——, and S. Sokolov, 2001: Baroclinic transport variability of the Antarctic Circumpolar Current south of Australia (WOCE repeat section SR3). *J. Geophys. Res.,* **106** (C2), 2815–2832.

Roach, A. T., K. Aagaard, C. H. Pease, S. A. Salo, T. Weingartner, V. Pavlov, and M. Kulakov, 1995: Direct measurements of transport and water properties through the Bering Strait. *J. Geophys. Res.,* **100** (C9), 18 443–18 457.

Roemmich, D., 2007: Physical oceanography: Super spin in the southern seas. *Nature,* **449,** 34–35.

Roether, W., R. Schlitzer, A. Putzka, P. Beining, K. Bulsiewicz, G. Rohardt, and F. Delahoyde, 1993: A chlorofluoromethane and hydrographic section across Drake Passage: Deep water ventilation and meridional property transport. *J. Geophys. Res.,* **98,** 14 423–14 435.

Sallée, J., K. Speer, S. Rintoul, and S. Wijffels, 2010: Southern Ocean thermocline ventilation. *J. Phys. Oceanogr.,* **40,** 509–529.

Sallée, J. B., K. Speer, and S. R. Rintoul, 2011: Mean-flow and topographic control on surface eddy-mixing in the Southern Ocean. *J. Mar. Res.,* **69,** 753–777.

Sasaki, H., M. Nonaka, Y. Masumoto, Y. Sasai, H. Uehara, and H. Sakuma, 2008: An eddy-resolving hindcast simulation of the quasi-global ocean from 1950 to 2003 on the Earth Simulator. *High Resolution Numerical Modeling of the Atmosphere and Ocean,* W. Ohfuchi and K. Hamilton, Eds., Springer, 157–185.

Siedler, G. T., J. Muller, R. Onken, M. Arhan, H. Mercier, B. A. King, and P. M. Saunders, 1996: The zonal WOCE sections in the South Atlantic. *The South Atlantic, Present and Past Circulation,* G. Wefer, et al., Eds., Springer, 83–104.

Sloyan, B. M., and S. R. Rintoul, 2001a: Circulation, renewal and modification of Antarctic mode and intermediate water. *J. Phys. Oceanogr.,* **31,** 1005–1030.

——, and ——, 2001b: The Southern ocean limb of the global deep overturning circulation. *J. Phys. Oceanogr.,* **31,** 143–173.

Speer, K. G., and W. Zenk, 1993: The flow of Antarctic Bottom Water into the Brazil Basin. *J. Phys. Oceanogr.,* **23,** 2667–2682.

——, S. R. Rintoul, and B. Sloyan, 2000: The diabatic Deacon cell. *J. Phys. Oceanogr.,* **30,** 3212–3222.

Spreen, G., L. Kaleschke, and G. Heygster, 2008: Sea ice remote sensing using AMSR-E 89-GHz channels. *J. Geophys. Res.,* **113,** C02S03, doi:10.1029/2005JC003384.

Tandon, A., and C. Garrett, 1996: On a recent parameterization of mesoscale eddies. *J. Phys. Oceanogr.,* **26,** 406–411.

Toggweiler, J. R., and B. Samuels, 1998: On the ocean's large-scale circulation near the limit of no vertical mixing. *J. Phys. Oceanogr.,* **28,** 1832–1852.

Toole, J. M., and B. A. Warren, 1993: A hydrographic section across the subtropical South Indian Ocean. *Deep Sea Res. I,* **40,** 1973–2019.

Treguier, A. M., I. M. Held, and V. D. Larichev, 1997: Parameterization of quasigeostrophic eddies in primitive equation ocean models. *J. Phys. Oceanogr.,* **27,** 567–580.

Tsimplis, M. N., S. Bacon, and H. L. Bryden, 1998: The circulation of the subtropical South Pacific derived from hydrographic data. *J. Geophys. Res.,* **103** (C10), 21 443–21 468.

Tziperman, E., 1988: Calculating the time-mean oceanic general circulation and mixing coefficients from hydrographic data. *J. Phys. Oceanogr.,* **18,** 519–525.

Urakawa, L. S., and H. Hasumi, 2012: Eddy-resolving model estimate of the cabbeling effect on the water mass transformation in the Southern Ocean. *J. Phys. Oceanogr.,* **42,** 1288–1302.

Walin, G., 1982: On the relation between sea-surface heat flow and thermal circulation in the ocean. *Tellus,* **34,** 187–195.

Webb, D. J., and N. Suginohara, 2001: Oceanography: Vertical mixing in the ocean. *Nature,* **409,** 37.

Whitworth, T., B. A. Warren, W. D. Nowlin, S. B. Rutz, R. D. Pillsbury, and M. I. Moore, 1999: On the deep western-boundary current in the Southwest Pacific Basin. *Prog. Oceanogr.,* **43,** 1–54.

Wijffels, S. E., J. M. Toole, and R. Davis, 2001: Revisiting the South Pacific subtropical circulation: A synthesis of World Ocean Circulation Experiment observations along 32°S. *J. Geophys. Res.,* **106** (C9), 19 481–19 513.

Wunsch, C., 1999: Where do ocean eddy heat fluxes matter? *J. Geophys. Res.,* **104** (C6), 13 235–13 249.

——, 2006: *Discrete Inverse and State Estimation Problems: With Geophysical Fluid Applications.* Cambridge University Press, 371 pp.